Progress in Natural Science: Materials International 2013;23(3):222–234

Chinese Materials Research Society

Progress in Natural Science: Materials International

www.elsevier.com/locate/pnsmi
www.sciencedirect.com

REVIEW

Nanoscale electron tomography and atomic scale high-resolution electron microscopy of nanoparticles and nanoclusters: A short survey

John Meurig Thomas*, Paul A. Midgley, Caterina Ducati, Rowan K. Leary

Department of Materials Science and Metallurgy, University of Cambridge, Pembroke Street, Cambridge, CB2 3QZ, UK

Received 26 December 2012; accepted 12 March 2013
Available online 7 June 2013

KEYWORDS

Nanoclusters;
Nanoparticles;
Atomic structure;
Electron tomography;
Aberration-corrected electron microscopy

Abstract The outstanding merits of scanning transmission electron tomography as a technique for the investigation of the internal structure and morphology of nanoparticle and nanocluster materials are summarized with the aid of numerous typical illustrations. Reference is made also to the significant advances that have arisen in probing ultrastructural characteristics of nanoscale solids using aberration-corrected (AC) electron microscopy (EM). Information of a unique kind may be retrieved by combining the imaging and analytical power of ACEM.

1. Introduction

So widespread in hospitals throughout the world is the use of CT scanners (where CT stands for computerised tomography) that the general public is now aware that this procedure entails taking a variety of X-ray images through a range of accurately aligned settings which, in turn, yield a three-dimensional (3D) picture of the subject under investigation.

Scientists interested in the nanostructures of a variety of solid objects also use tomographic approaches. Sometimes they use X-rays, but nowadays, increasing use is being made of electron tomography (ET), the essence of which is summarised below. Before doing so, however, we recall that, with the greater availability of synchrotron sources, short wavelength X-rays are used to determine the 3D structures of small objects. X-rays possess several advantages over electrons as probing radiation, principally because they have greater penetrating power. They have, however, some disadvantages in that they are far less readily focusable than electrons. Notwithstanding the ever-increasing improvements that are being made in the construction of Fresnel lenses for focusing X-rays, ET has at present far greater resolving power than its X-ray counterpart. A summary of the nature of the relative strengths and advantages of each technique is given in an earlier article by two of us [1], from which some parts of this review are taken. For completeness, some illustrative examples of X-ray tomographic reconstructions are given in Fig. 1.

*Corresponding author.
E-mail address: jmt2@cam.ac.uk (J.M. Thomas).

Peer review under responsibility of Chinese Materials Research Society.

ELSEVIER Production and hosting by Elsevier

1002-0071 © 2013 Chinese Materials Research Society. Production and hosting by Elsevier B.V. All rights reserved.
http://dx.doi.org/10.1016/j.pnsc.2013.04.003

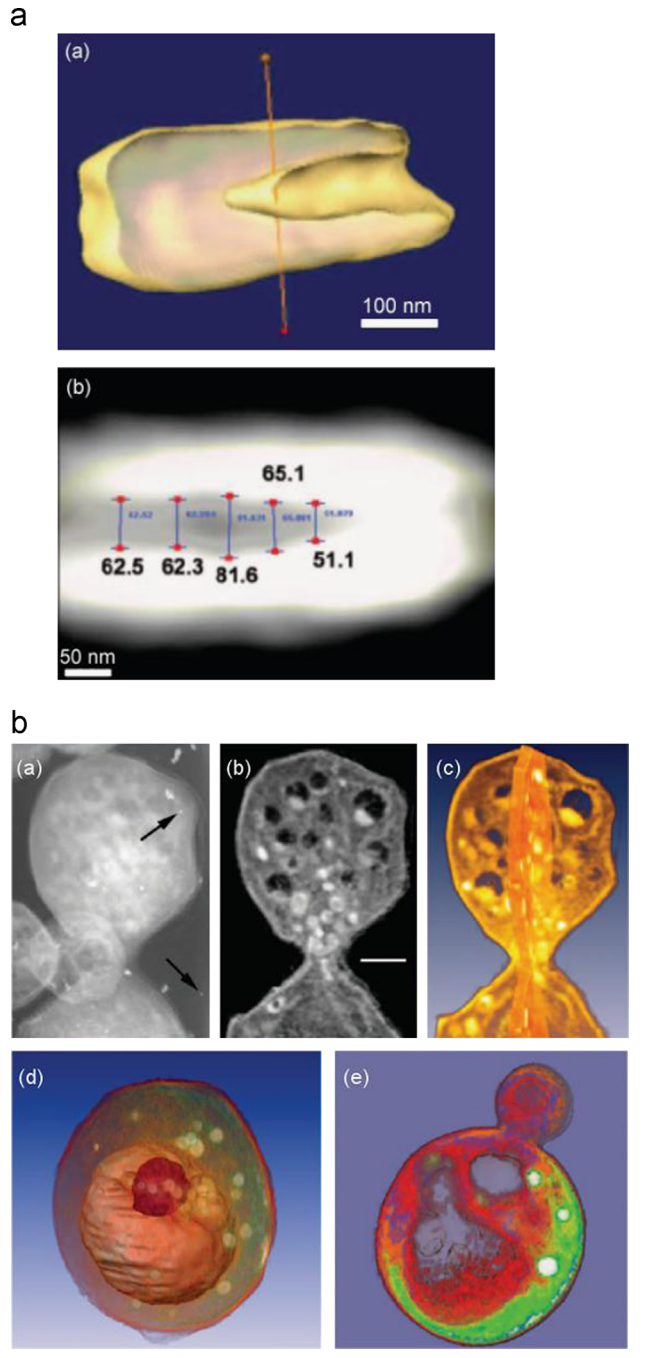

Fig. 1 (a) Reconstructed X-ray tomogram illustrating (top) the side view of a reconstructed tungsten plug and (bottom) the measurement of the size of the keyhole. Reproduced from [2]. (b) X-ray tomography of whole yeast cells showing (top) a single projection image of a rapidly frozen budding yeast, a section through a tomographic reconstruction of the yeast (scale bar = 0.5 mm) and a volume-rendered view of the reconstruction. The bottom two panels show a volume-rendered image with the nucleus (purple), vacuole (pink) and lipid droplets (white) and a colour-coded reconstruction of a budding yeast with lipid droplets (white), vacuoles (grey) and numerous other subcellular structures coloured shades of green, orange and red. Reproduced from [3].

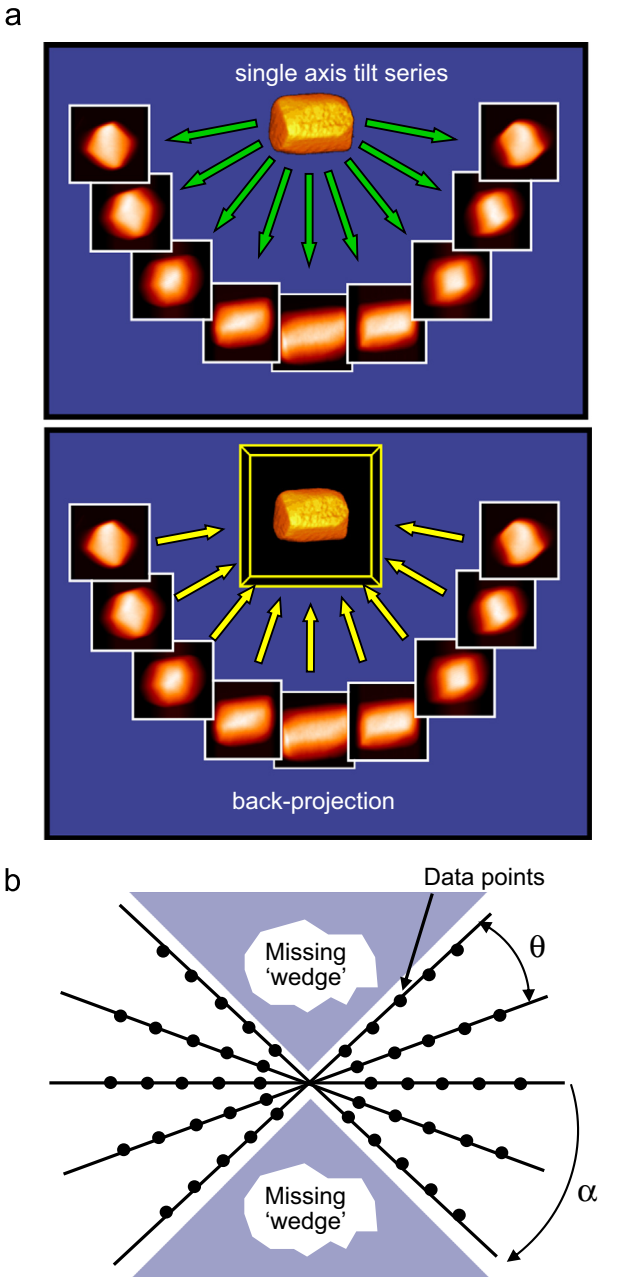

Fig. 2 (a) The essence of tomographic reconstruction. The top schematic shows a series of projections of an object at different angles and the bottom schematic depicts how these images are back-projected into space, wherein the conglomerate sum of the back-projections defines the reconstructed object. (b) A Fourier space representation of the angular series of images (projections) in (a), illustrating the finite angular increment θ between images, and the maximum angular range α to which images are recorded, leading to incomplete sampling; the latter giving rise to a large 'missing wedge' of unsampled information. Each data point is represented schematically, showing that the radial sampling of Fourier space leads to a greater sampling density around the centre of Fourier space, meaning that lower spatial frequency information is oversampled relative to high spatial frequency information.

In recent years the remarkable resolving power of the electron microscope has been enhanced still further by the introduction of aberration-corrected optics. This has led to an ability to resolve directly structural detail at the atomic level, with clarity and precision, leading to new insights into the physical and chemical behaviour of nanoscale structure and devices. Later in this review,

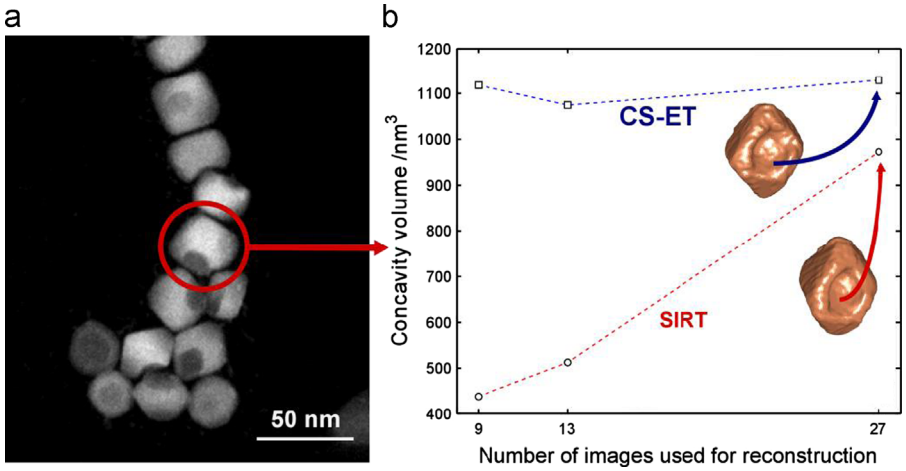

Fig. 3 (a) HAADF-STEM image of concave iron oxide nanoparticles taken from an ET tilt-series. (b) Quantification of the concavity volume of the nanoparticle indicated in (a), from CS-ET and SIRT reconstructions. Reproduced from [11].

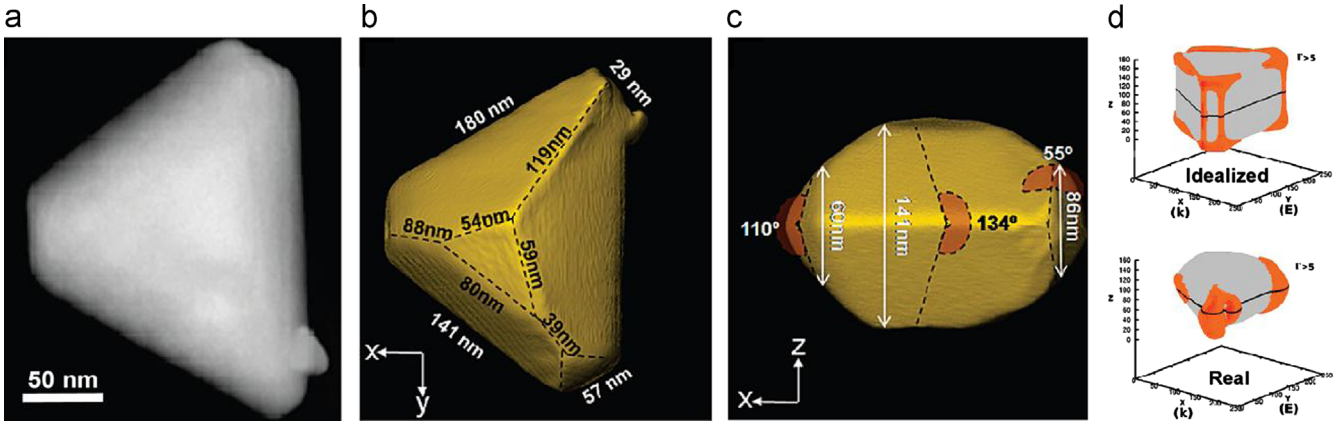

Fig. 4 (a) HAADF-STEM image of an Au nanoparticle. (b,c) Surface-rendered views of a reconstructed Au nanoparticle, with dimensions indicated. (d) 3D simulations for the real (using the tomogram) and an idealised (estimated from a single image) nanoparticle, showing regions of high electromagnetic-field enhancement (marked in orange). Reproduced from [35].

we give a number of examples of high resolution imaging, but focus first on the principles and recent applications of ET.

2. The essence of electron tomography (ET) using a scanning transmission electron microscope

2.1. Principles [1]

Tomography, which involves generating a reconstruction from projections of an object viewed from different directions (see Fig. 2(a)), derives from the mathematical principles described by Radon just over ninety years ago [4]. The Radon transform is defined as a mapping into so-called 'Radon space' of a function describing a real space object, by the projection, or line integral, through that function along all possible lines. Thus, given a sufficient number of projections, an inverse Radon transform (or back-projection) of this space should reconstruct the object. In practice, however, the sampling will always be limited, the inversion will be imperfect, and the goal then becomes to achieve the 'best' reconstruction of the object given the limited experimental data. This is particularly so in ET, where the specimen is rotated in order to obtain projections at different angles, because the limited space within the microscope objective lens frequently prevents rotation of the sample holder through the full angular range. This leaves a 'missing wedge' of information unsampled by the tilt-series of images (projections) (see Fig. 2(b)). Additionally, a limit on the total number of tilt-series images that can be acquired may be imposed by the electron beam sensitivity of the sample. This is less of a problem for many samples in the materials sciences, such as metals or alloys, which are often relatively robust under the electron beam, but is frequently a limiting factor in the biological sciences, where 'low-dose' acquisition schemes must be followed.

Another important concept in tomography is the so-called 'central slice theorem.' This says that a projection of an object at a given angle in real space is a central section through the Fourier transform of that object [5]. Hence once can see how by recording multiple projections at different angles, many Fourier sections will be sampled, and in principle tomographic reconstruction is possible from an inverse Fourier transform. This approach is known as direct Fourier reconstruction [5,6]. Although elegant,

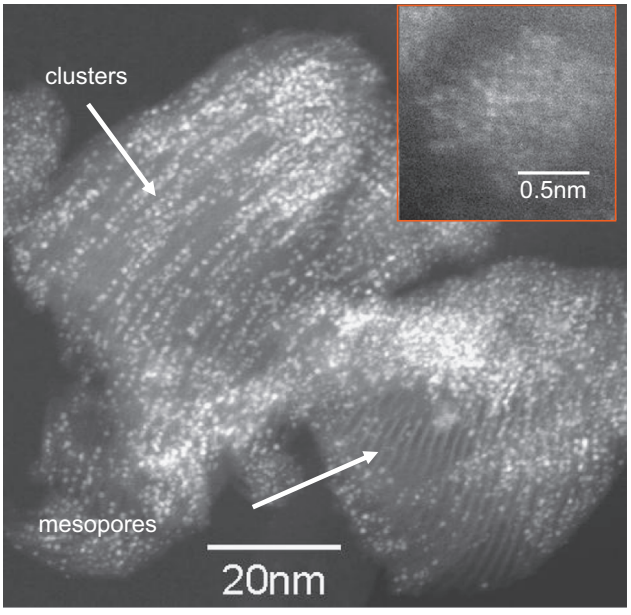

Fig. 5 HAADF-STEM image of $Ru_{10}Pt_2$ nanoclusters on MCM-41 mesoporous silica. The inset shows one of the particles at high magnification showing individual atoms and atom clusters. Reproduced from [39].

and used in the first demonstration of ET [7], Fourier reconstruction methods have for a long time been seen as computationally intensive and difficult to implement, and simpler real space back-projection methods [8–10] have been preferred. With recent computational advances however, Fourier based methods have seen a resurgence, being used in some modern algorithms that are capable of providing high-fidelity reconstructions [11,12].

The method of back-projection is based on inverting the set of recorded images, projecting each image back into an object space at the angle at which the original image was recorded. Using a sufficient number of back-projections, from different angles, the superposition of all the back-projected 'rays' will reconstruct the original object, see again Fig. 2(a). The mathematical principles of tomographic reconstruction are detailed in many books, such as those by Kak and Slaney [13], Herman [14] and Deans [5]. Foundational reviews of reconstruction methods specifically with regards to ET have been given by, for example, Penczek [15] and in the book edited by Frank [16].

Reconstructions using back-projection often appear blurred with fine spatial detail reconstructed poorly. This is an effect of the uneven sampling of spatial frequencies in the ensemble of original projections. As can be seen in Fig. 2(b), there is proportionately greater sampling of data near the centre of Fourier space compared with the periphery. It is possible partially to rebalance the frequency distribution in Fourier space by using a weighting filter: a radially linear function in Fourier space, zero at the centre and a maximum at the edge. This improved reconstruction approach is known as weighted back-projection [10,17].

Further enhancements in fidelity of tomographic reconstructions may be obtained via the use of iterative reconstruction algorithms [18–22]; for recent advanced algorithms in ET, see e.g. [11,12,23,24]. In iterative reconstruction methods, the reconstruction can be improved by noting that each recorded image is a 'perfect' reference projection. If an (imperfect) reconstruction is re-projected back along the original projection direction, the re-projections, in general, will not

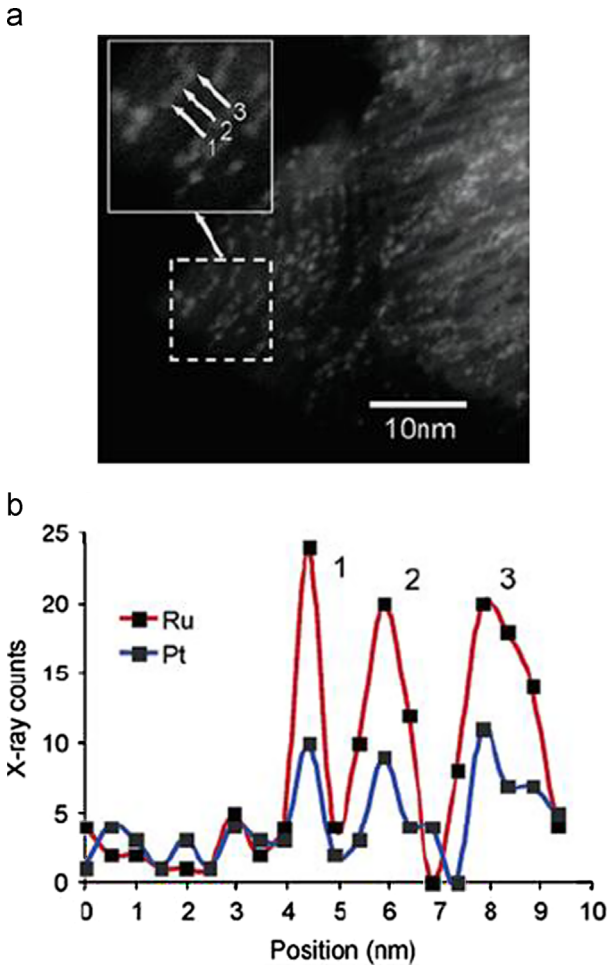

Fig. 6 (a) HAADF-STEM image of Ru–Pt–based catalyst. The inset shows the particles studied by X-ray microanalysis. X-ray spectra recorded approximately every 0.5 nm led to a compositional profile shown in (b). From the area under the curve in the region of the three nanoparticles, the ratio of Ru:Pt for each particle is consistent with the 5:1 ratio expected from the synthesis. Reproduced from [40].

be identical to the original images. The difference, characteristic of the deficiency of the reconstruction, can be back-projected to generate a 'difference' reconstruction, which can be used to correct the original reconstruction, to constrain the reconstruction to agree better with the original set of images. A single operation will not fully correct the reconstruction and the comparison must be repeated until a 'best' solution is reached. In conjunction with this difference-based iterative refinement, the fidelity of a reconstruction can also be improved by incorporating some additional prior-knowledge about the object during the reconstruction process. One approach to this is 'discrete' tomography, which is described elsewhere [23,25]. Another is the so-called procedure of 'compressed sensing,' which has been the recent focus of attention in our group, and which we recall below.

2.2. *Compressed sensing electron tomography (CS-ET) [26]*

The principles of image compression (e.g., as used for JPEG formats), where images are retrieved from their compressed form without significant information loss, provide an alternative basis for 3D reconstruction from very limited data sets as we have in ET and found often in magnetic resonance imaging [27] and X-ray

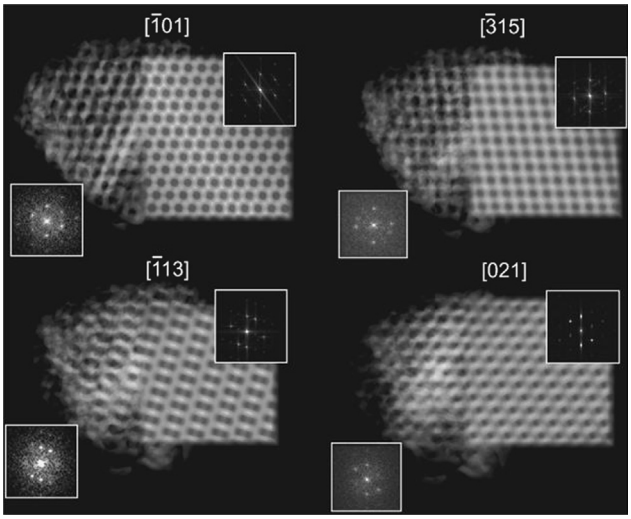

Fig. 7 A montage of tomographic projections of MCM-48 silica (with corresponding simulations and Fourier transforms) shown at major zones axes as the 3D tomographic reconstruction is rotated about a $<112>$ zone axis. Reproduced from [41].

CT [28]. The method known as 'compressed sensing' (CS) is able to recover a high-fidelity reconstruction from a highly under-sampled data set if the object to be reconstructed is 'sparse,' in this context meaning having relatively few non-zero pixels (or voxels) [29,30]. The sparsity may be in the same space as the reconstruction (typically real space) or in some other space linked by a known transform (e.g., in a gradient domain). If the object can be approximated in a sparse way, it is said to be 'compressible.' To ensure a high-fidelity reconstruction, free from aliasing artefacts, for example, sampling of the object should be performed in a random (or near-random) fashion [27]. A tilt-series, as acquired in ET, has been shown to provide a sampling scheme that, although clearly not random, results in aliasing artefacts that are sufficiently 'noise-like' that they can be removed by CS. Thus for ET, the CS reconstruction proceeds by finding the sparsest representation of the object to be reconstructed, subject to re-projections of that object best-fitting the original microscope images. Here, the knowledge that the object is in some sense 'sparse' provides the extra prior information that improves the reconstruction.

Recently, the authors, in collaboration with the Gladden group in Cambridge (especially D.J. Holland) have shown that CS applied to ET can yield high-fidelity 3D reconstructions from

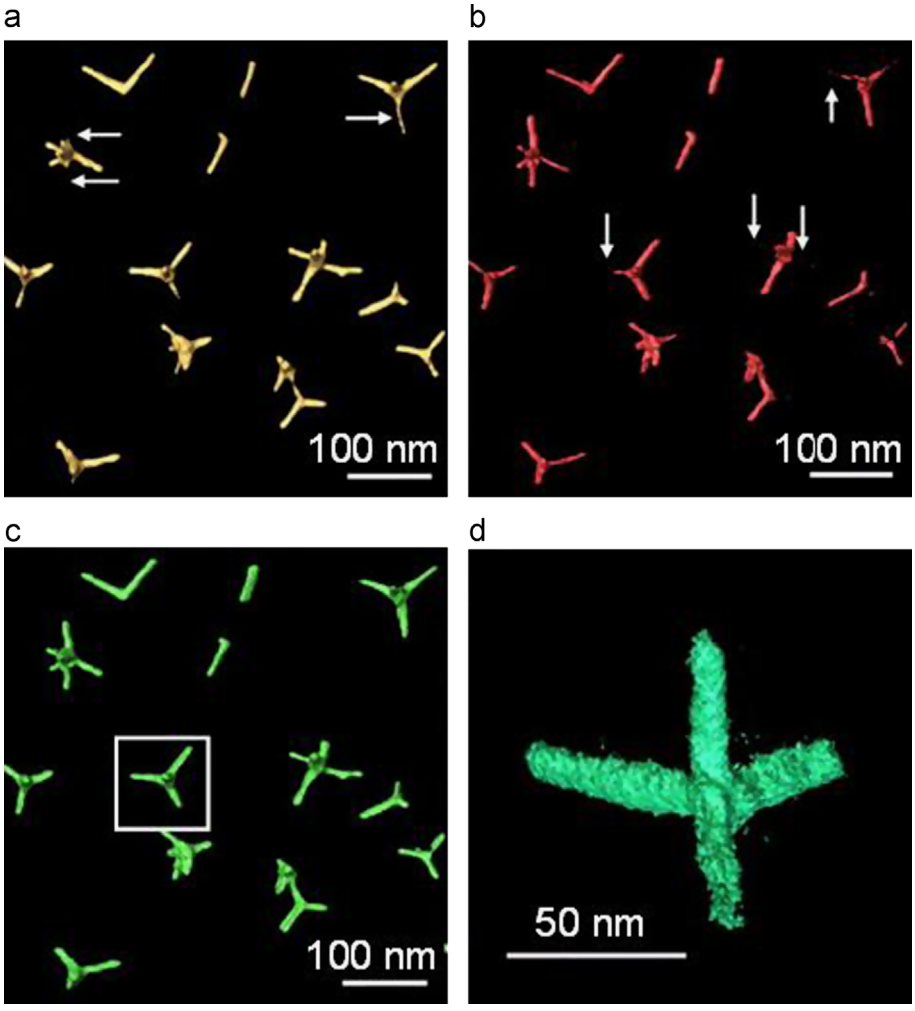

Fig. 8 3D reconstruction of a dual-axis tilt series of CdTe tetrapods. (a) is a reconstruction of a single tilt series and shows that some of the legs of the tetrapods are poorly reconstructed, due to the missing wedge, as indicated by the arrows. (b) is a reconstruction of a tilt series recorded about an axis perpendicular to that in (a) showing poorly reconstructed legs, again indicated by the arrows. (c) is a dual axis reconstruction of the two data sets illustrating that all legs are well reconstructed. (d) Detailed view of the tetrapod selected in (c). Reproduced from [43].

very few images. One example, a CS-ET reconstruction of concave iron oxide nanoparticles [11], illustrated in Fig. 3, demonstrates how, compared with the standard iterative reconstruction algorithm in ET (known as the simultaneous iterative reconstruction technique, SIRT [20]), CS-ET provides a faithful reconstruction of the octahedral morphology and a robust quantitative measurement of the nanoparticle concavity, even from a tilt-series composed of only nine images. Knowledge of precise 3D morphology, such as the concavity, is key for application of the particles in drug delivery and photocatalysis [31].

Compared with discrete tomography, CS-ET potentially offers a more flexible approach to how constraints can be applied. For example, for homogeneous objects with sharp boundaries, sparsity may be found in the gradient domain by minimising the so-called 'total variation' [11,24], or for more diffuse objects (e.g., those with compositional gradients), wavelet representations can be used [32,33], as they are for JPEG compression in digital photography. Although still in its infancy, we expect CS-ET to be adopted widely in the future. In particular, the ability of CS-ET to yield high-fidelity reconstructions from relatively few images should prove to be of great benefit in the study of beam-sensitive samples, or where total acquisition time is limited.

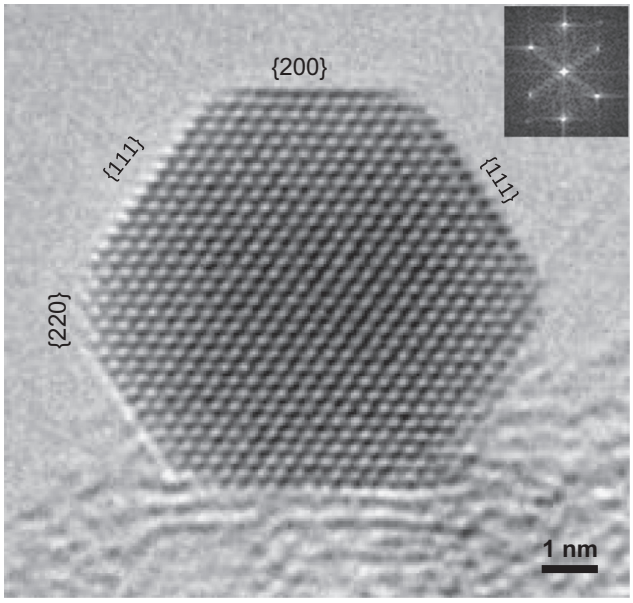

Fig. 9 High resolution TEM image of an AgI nanoparticle recorded parallel to the <110> zone axis, exhibiting a truncated octahedral morphology. The planes seen in the figure are labelled. The inset shows the FFT of the nanoparticle.

2.3. *Nanoparticles with plasmonic responses[26]*

Nanoscale solids in the range 1–100 nm are well-known to exhibit chemical properties that are critically dependent upon their shape and morphology [1,34]. Whereas conventional scanning transmission electron microscopy (STEM) and other high-resolution imaging techniques cannot reveal directly the 3D morphology of such nanoparticles, the ET approach outlined above can. A prime example is a study [35] linking the plasmonic response of an Au nanoparticle to its true morphology. STEM tomography showed the nanoparticle to have a 3D shape markedly different from the one that would be inferred from a single 2D image (Fig. 4(a)–(c)). Using the ET reconstruction, the morphology of the nanoparticle was encoded as finite elements and used as input to 3D electrodynamics simulations [35]. By comparing simulations performed using a model based on the true irregular morphology, with those using an idealised shape assumed from a 2D (S)TEM image, dramatic differences in the predicted optical properties were found (Fig. 4(d)).

2.4. *Revealing the tortuosity and pore-structure of mesoporous silica*

Ordered mesoporous silicas are excellent supports for a range of nanoparticle and nanocluster bimetallic catalysts of high activity and selectivity in the hydrogenation of a range of organic molecules [36–38]. The catalytic variant of cubic mesoporous silica known as MCM-48—there is a hexagonal variant known as MCM-41, where MCM stands for mobil catalytic material—has a complex gyroid-like 3D pore network. This cubic phase, as a catalyst support, is intrinsically superior to its hexagonal analogue, MCM-41, in that pores run in three mutually perpendicular directions in the former, whereas they run in only one direction in the latter. Clearly the diffusion of reactants to, and products away from the minute nanoclusters anchored to the

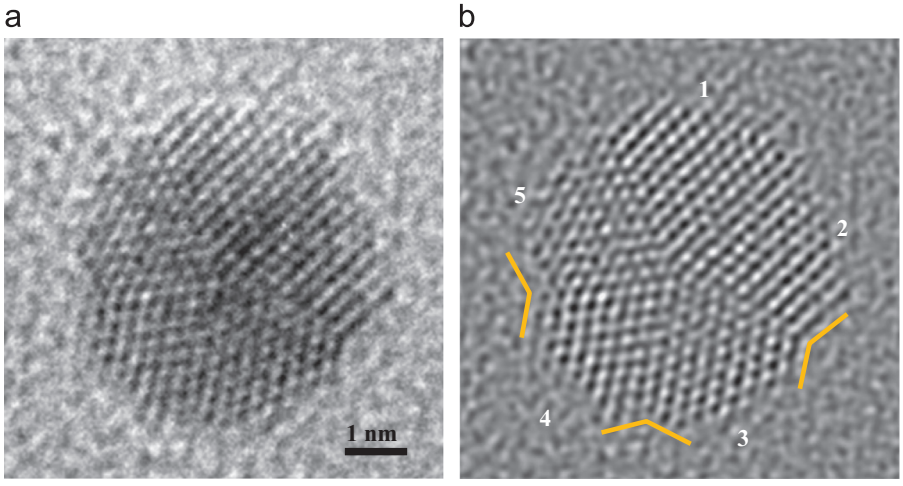

Fig. 10 (a) High resolution TEM image of an Au nanoparticle exhibiting five-fold twinning. The five sectors (labelled) of the twinned particle are revealed more clearly in (b) which is a Fourier-filtered version of the image in (a). Re-entrant facets are marked with chevrons.

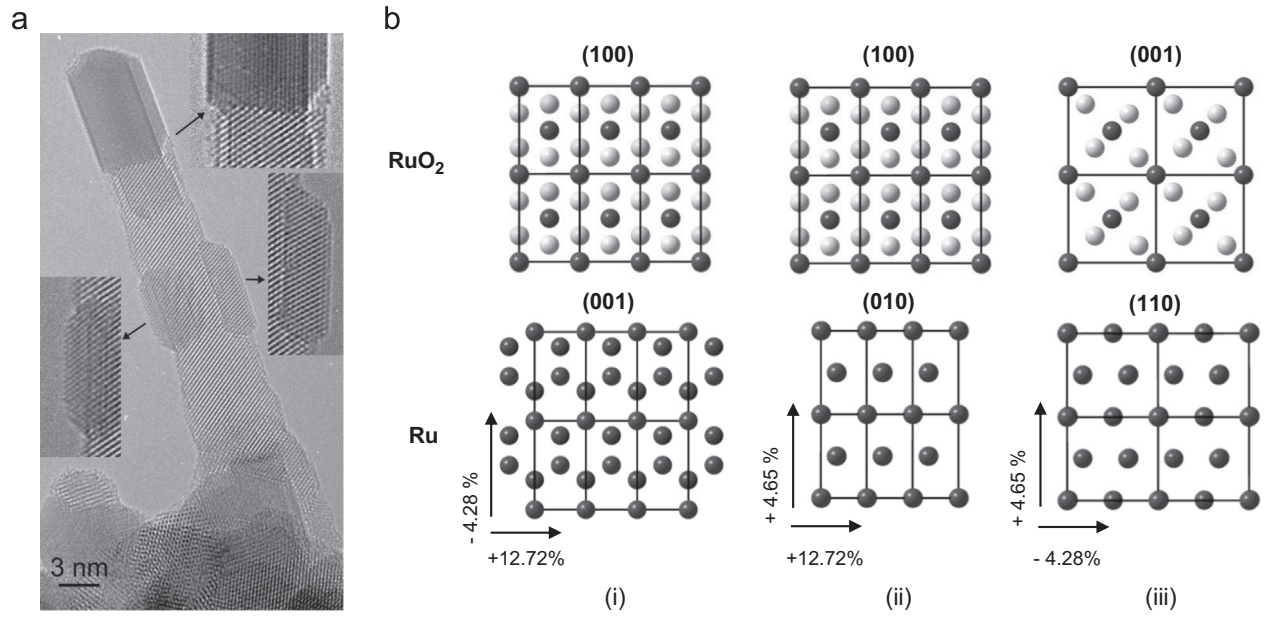

Fig. 11 (a) High resolution TEM image of a RuO_2 nanorod decorated with Ru clusters. Edge dislocations can be seen at interface between Ru and RuO_2 for the cluster on the right-hand side of the rod. (b) The three orientation relationships of RuO_2 and Ru lattices are shown, in plan view (Ru atoms in dark grey and O atoms in light grey). The values of the mismatch are given for the Ru lattice relative to the RuO_2 substrate. Reproduced from [55].

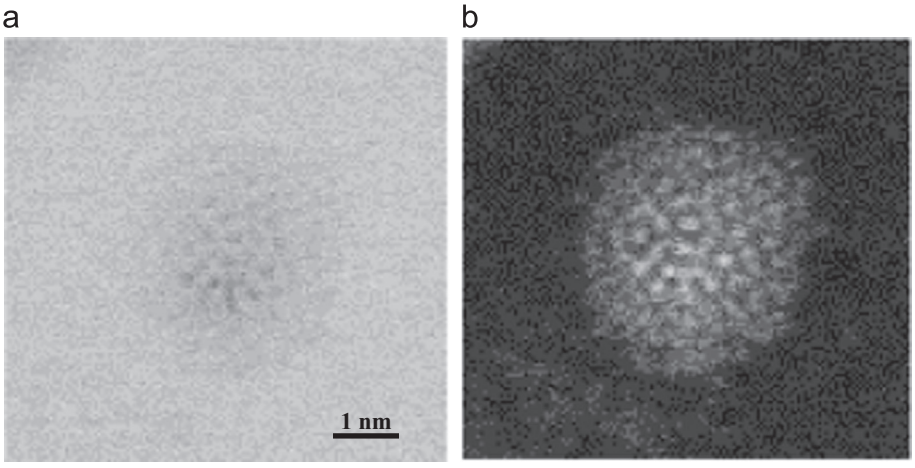

Fig. 12 Aberration-corrected (a) BF- and (b) ADF-STEM images of a Ga-Pd nanoparticle particle, recorded simultaneously. The contrast and clarity of the ADF image is considerably higher than that of the BF image.

mesoporous silica is much facilitated using MCM-48 supports. To fix our ideas, Figs. 5 and 6 show STEM, high-angle annular dark-field (HAADF) images – see Section 3 for more details—of typical Ru-Pt nanocluster selective hydrogenation catalysts.

Returning to the investigation of the porosity of the mesoporous silica support, a significant advantage of studying such systems using ET is the ability to visualise the pore structure directly. As well as providing a model-independent structure solution, tomography, being a direct imaging technique, further provided the opportunity to reveal any deviations from the perfect crystal structure, such as twin boundaries. A series of 158 HAADF-STEM images was acquired every 1° between −78° and +79°. Fig. 7 shows a montage of voxel projections computed from a 3D tomographic reconstruction of a sub-100 nm particle of MCM-48 silica [41]. Each projection is at a zone axis encountered when rotating about a <112> axis through a symmetry-independent sector of reciprocal space. A {112} plane, whose normal is vertical in the plane of the paper, is common to all projections. On the right of each image is a simulation of the MCM-48 structure based on an approximate gyroid surface. Power spectra (computed diffractograms) for both experiment and simulation are shown as insets. The agreement between experiment and simulation is remarkably consistent for each projection. Based on the direct 3D information available from ET, the structural model was revised to better match the observed pore size and distribution. The original model was based on studies [42] in which the complementary pore sizes of MCM-48 were determined based primarily on pore volumes modelled from nitrogen gas

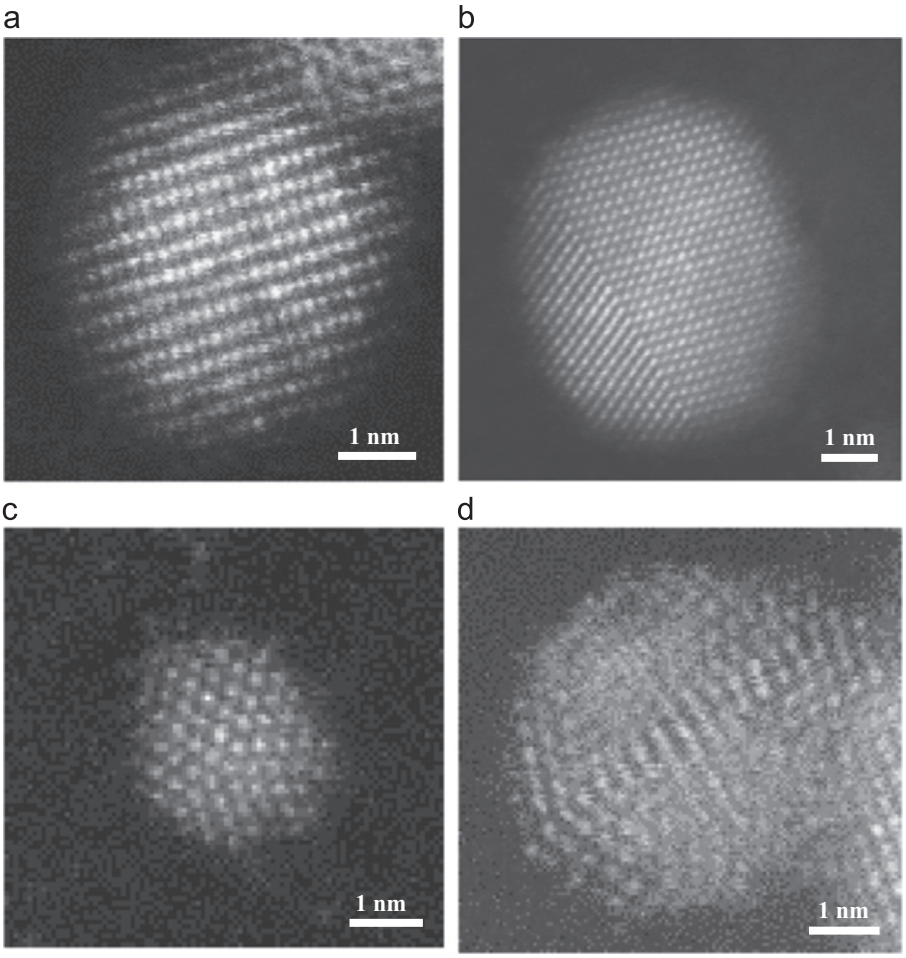

Fig. 13 A montage of aberration-corrected ADF-STEM images of different morphologies of gold nanoparticles. (a) shows a single crystal nanoparticle, (b) a singly-twinned nanoparticle, (c) a small decahedral nanoparticle in five-fold orientation (image courtesy of J.S. Barnard), and (d) an icosahedral nanoparticle, oriented parallel to its two-fold axis.

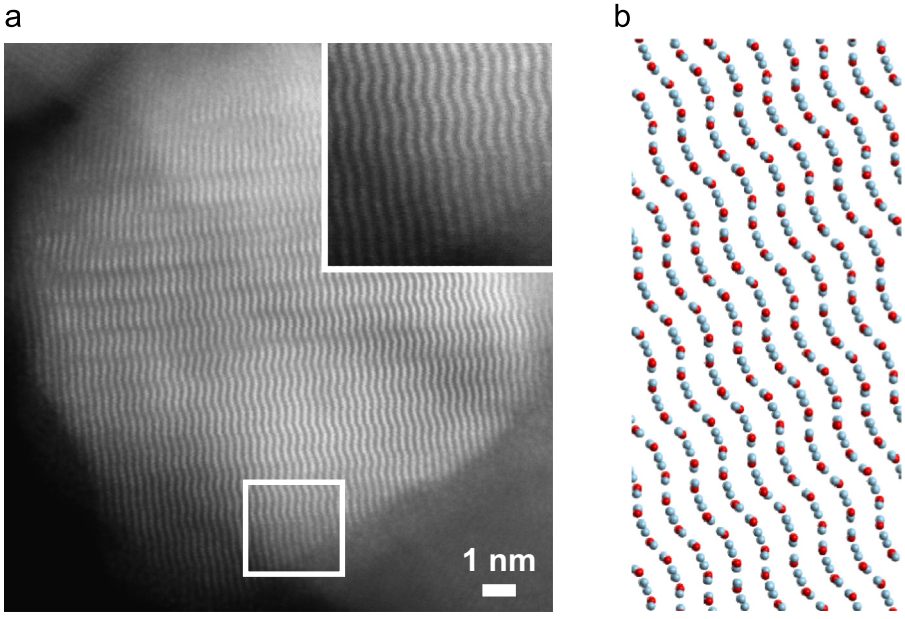

Fig. 14 (a) Aberration-corrected ADF-STEM image of a $GaPd_2$ nanoparticle viewed parallel to the [120] zone axis. Notice how the 'waviness' of the projected structure reduces significantly at the nanoparticle's edge—highlighted further in the inset. (b) The $GaPd_2$ structure projected parallel to the [120] zone axis, Ga in red, Pd in light blue.

adsorption–desorption experiments; in the future, direct structural measurements available with STEM tomography should overcome some of the limitations of such model-dependent analyses.

A concluding example of 3D nanostructure determination is given in Fig. 8, which demonstrates the improvements in fidelity that can be realised when a tomographic reconstruction is based on a dual-axis series [43]. A single-axis reconstruction of CdTe tetrapods reveals some legs have not been reconstructed, due to the effects of the missing wedge. By taking mutually perpendicular tilt series and reconstructing their combination, the size of the missing wedge is reduced and the structure of the tetrapods is fully revealed.

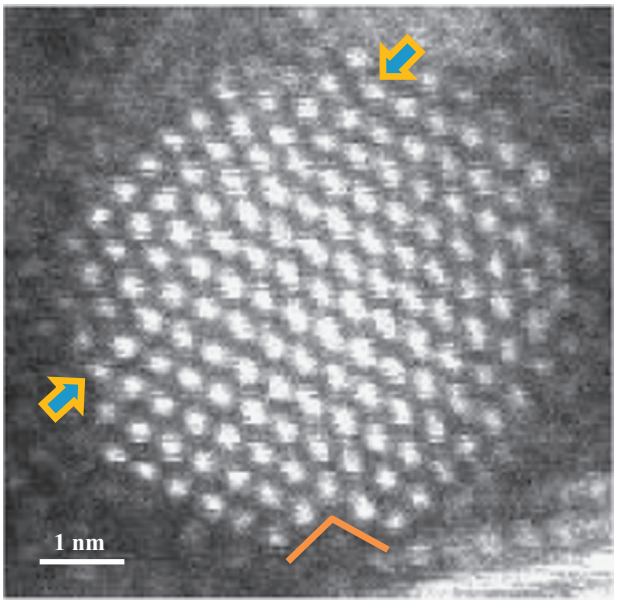

Fig. 15 Aberration-corrected ADF-STEM image of a small $GaPd_2$ nanoparticle showing a re-entrant facet (marked with a chevron) and a single twin boundary (arrowed).

3. Atomic-scale high resolution electron microscopy (HREM)

Numerous recent articles and books have dealt with the principles of HREM and with the particular variant known as annular dark-field (ADF) or high-angle annular dark-field HAADF) scanning transmission electron microscopy (STEM)—see e.g. [44–47]. With the advent of aberration-corrected optics for HREM, a new era in atomic-scale imaging has arrived. In this short survey we aim to reach two goals: first a set of illustrations of the quality of such atomic-scale images to metal nanoclusters and nanoparticles is given; second, we enter into the present speculative field of ascertaining what feature of these nanocatalysts is likely to hold the key to the root cause of the exceptional catalytic activity of such materials as nano-gold on various oxide or carbonaceous supports.

Firstly, it is important to stress that a wealth of information can be obtained from conventional high resolution micrographs recorded from instruments without aberration correction, and we begin this section with a few examples. Fig. 9 shows a high resolution image recorded on a conventional TEM using a relatively high beam energy of 400 keV—this approach, where the higher beam energy yields a smaller electron wavelength, was for a long time the best available method to improve the 'point' resolution. The image is of a single AgI nanoparticle sitting on a carbonaceous support. The nanoparticle is oriented such that the electron beam is parallel to the $<110>$ zone axis, as confirmed by the fast Fourier

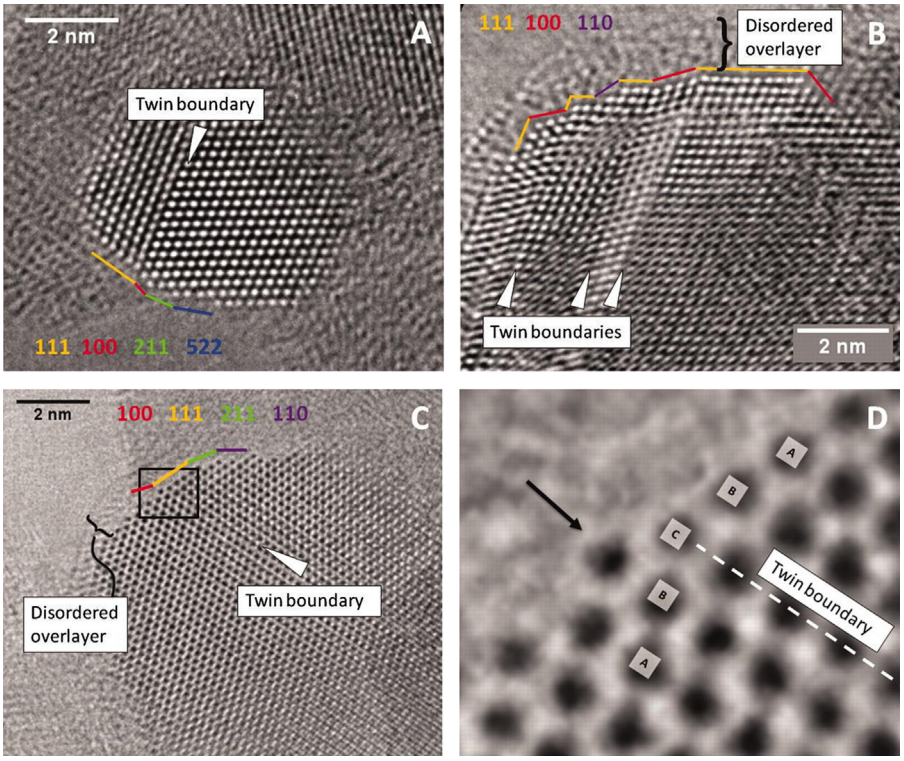

Fig. 16 Aberration-corrected TEM images of Cu particles in a high-performance $Cu/Zn/Al_2O_3$ catalyst, showing significant faceting, twinning and a disordered over-layer. (d) is a magnified region of the area marked in (c). Reproduced from [64].

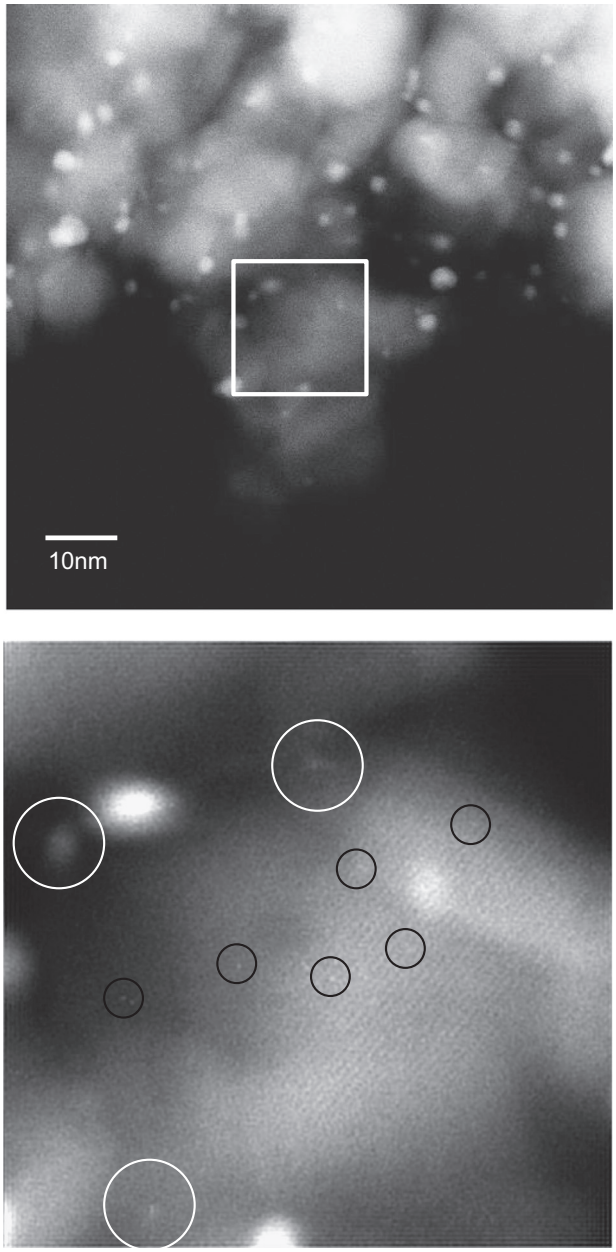

Fig. 17 (a) Aberration-corrected HAADF-STEM images of an gold/titania catalyst. (b) Magnified part of (a) showing single gold atoms (black circles) and gold clusters (white circles) Reproduced from [67]. Images courtesy of P.L. Gai.

transform (FFT) of the image shown as an inset. The nanoparticle shows a truncated octahedral morphology, with well-defined {100} and {111} facets. Phase contrast such as that seen in this image can be beneficial when investigating the structure of low atomic number material. In this case, it is clear that the carbonaceous support directly below the nanoparticle in the figure is of a graphitic nature with 3–4 layers of graphite apparently coherent with the {200} planes of the nanoparticle. However, phase-contrast images, particularly those from microscopes that are not aberration corrected, also need to be interpreted with caution as rapid contrast reversals can occur with change of defocus and specimen thickness.

Fig. 10 shows an HR-TEM image of a gold nanoparticle that exhibits a more complex, five-fold twinned structure. Here successive cyclic twinning on the {111} planes leads to this pseudo-five-fold symmetric arrangement, where the five sectors are perhaps more easily seen in Fig. 10(b), which is a Fourier-filtered version of the raw image in Fig. 10(a). Successive twinning of a face centred cubic (fcc) lattice leads to a rotation between sectors of 70.53°, or 352.64° over the five sectors. Since this is less than the 360° needed for perfect closure there must inevitably be some distortion of the crystal lattice within the nanoparticle. Also indicated on the image are re-entrant {111} 'Marks-type' [48] facets that serve to reduce the surface-area-to-volume-ratio, and do so more favourably than truncation on {100} planes (as in Ino's decahedron [49]). The nature of the distortion in five-fold twinned nanoparticles has been the subject of many HREM studies and is a topic of much debate [50–53]. Recent work using aberration-corrected TEM asserts that the strain present in such nanoparticles is likely to have significant impact on surface adsorption properties, therefore being of high catalytic significance [54].

As a final example of conventional HR-TEM Fig. 11 shows that a thin ruthenium metal over-layer is seen to have grown on a ruthenium oxide nanorod, a composite structure with possible catalytic or energy applications [55]. In the image the ruthenium metal layer has grown in a semi-coherent fashion with the orientation relationships shown in Fig. 11b.

Whilst conventional HR-TEM can yield many images, when dealing with ultra-small nanoparticles or nanoclusters, ADF- or HAADF-STEM (ideally on an aberration-corrected instrument) can often offer some particular advantages. Fig. 12 shows simultaneously recorded (a) bright field (BF)- and (b) ADF-STEM images of a very small icosahedral Ga-Pd nanoparticle viewed close to its five-fold axis. In the phase-contrast BF image, the nanoparticle is barely visible and structural detail is very difficult to discern. ADF imaging however, is sensitive to the atomic number (Z) of the constituent atoms of the sample (in the limit of Rutherford scattering, a Z^2 relationship), and hence in the ADF image, the high Z nanoparticle is rendered clearly visible against the low atomic number silicon support film. To see detail in the BF image, phase contrast can be enhanced through a change in the image focus, but as noted previously, this can lead to significant changes in the image that require careful interpretation. A great strength of ADF-STEM is that the images are often 'directly interpretable' in terms of the projected atomic structure of the specimen. This is further demonstrated in Fig. 13, in which four different morphologies of gold nanoparticles are revealed with clarity. The gold nanoparticle in Fig. 13(a) is seen to be single-crystalline polyhedral, while in (b) a twin boundary separating two crystalline domains is clearly visible. (c) and (d) show examples of the two primary morphologies of five-fold twinned nanoparticles: (c) is a decahedral nanoparticle viewed close to its five-fold axis, and (d) is an icosahedral nanoparticle viewed close to its two-fold axis.

The addition of a second constituent species in nanoparticles and nanoclusters can significantly broaden the range of properties that are available [56]. Bimetallic systems are of particular interest for many catalytic applications [57,58]. The widened range of properties further heightens the need for judicious control of nanoparticle structure and for suitable characterisation methods. One promising route to achieving bimetallic systems with carefully controlled properties is to exploit the well-defined structures of intermetallic compounds, a prime example being the development of 'nano-sized' Ga-Pd intermetallic compounds for effecting selective hydrogenation reactions and other important processes such as methanol synthesis and methanol steam reforming [59,60]. Aberration-corrected (S)TEM can make important contributions to the knowledge-based development of such nanocatalysts, as exemplified in Figs. 14 and 15, where ADF-STEM has been used to

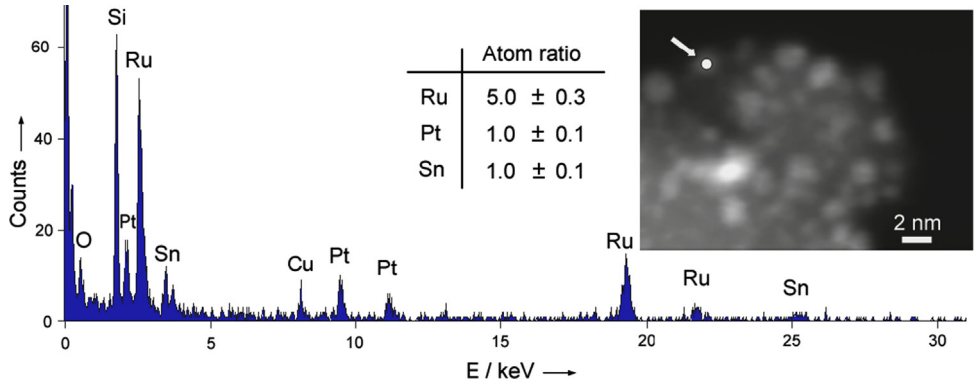

Fig. 18 Electron-induced X-ray emission spectrum of Ru_5PtSn nanoclusters on a mesoporous silica. The arrow in the inset identifies the particle for which this emission spectrum was recorded. The peak for Cu originates from the sample holder and grid. The tabulation refers to the results of 8 different X-ray emission spectra. Reproduced from [39].

reveal the atomic structure of $GaPd_2$ nanoparticles (see also Leary et al. [61,62]). The intermetallic $GaPd_2$ structure [63] is orthorhombic, but can be described as a distorted fcc structure. That distortion manifests itself as 'waviness' in the structure when viewed parallel to certain zone axes, which enables verification of the intermetallic state in the nanoparticles [61]. As an example, Fig. 14 shows a $GaPd_2$ nanoparticle viewed parallel to the [120] zone axis, where the 'wavy' nature of the projected structure is clear. However, the directly interpretable images provided by ADF-STEM are also extremely valuable in revealing deviations from the ideal structure – in Fig. 14 it can be seen that the 'waviness' reduces significantly at the nanoparticle's edge, which may be related to strain at the nanoparticle surface as well as segregation of Ga away from near-surface regions to form surface oxides [61]. With much smaller $GaPd_2$ nanoparticles, such as seen in Fig. 15, more detailed examination of the particle structure can take place. As seen with the Au nanoparticle in Fig. 10, the nanoparticle possesses re-entrant facets. This distinct faceting leads to a high proportion of low-coordinated surface atoms–environments quite distinct from a bulk terminated surface–the implications of which for Ga-Pd nanocatalysts are yet to be determined.

Also visible in Fig. 15 is a single twin boundary permeating the nanoparticle (arrowed), which causes perturbation of the nanoparticle surface. Such nano-crystalline defects are not insignificant, indeed they have been directly implicated in catalytic processes, as recently detailed for copper nanoparticles in the $Cu/ZnO/Al_2O_3$ catalyst system for methanol synthesis (see Fig. 16) [64]. It is believed that the surface structural irregularity functions as the locus of methanol synthesis and that traces of Zn at defect sites may also enhance catalytic activity.

In addition to catalytic nanoparticles, there is also increasing interest in few-atom nanoclusters, or indeed single atoms, as powerful catalysts [65,66]. The '*Z*-contrast' of aberration-corrected ADF-STEM is invaluable for enabling visualisation of such minute metallic catalysts supported on low atomic number supports, as exemplified in Fig. 17. There, single and pairs of gold atoms (circled in black) and gold clusters (circled in white) are clearly identified on the surface of titania, the nature of which are of particular interest for application in the selective oxidation of carbon monoxide [67].

We end this short survey with a brief example of the power of modern transmission electron microscopy not only to visualise the structure of nanoparticles and nanoclusters, but also to probe their chemical composition. Fig. 18 shows an energy dispersive X-ray spectrum from a single nanoparticle of Ru_5PtSn. The example spectrum was acquired by placing the electron probe on a single nanoparticle (shown by an arrow). Spectra from eight similar nanoparticles were averaged to produce a statistically significant chemical analysis, showing the nanoparticle composition indeed had, within 10% error, a 5:1:1 ratio as expected from the synthesis.

4. Conclusions

The remarkable physical and chemical properties exhibited by nanoparticles and nanoclusters can only be understood fully through a combination of bulk characterisation coupled with microscopic investigations using electron microscopy and related techniques. In this short review we have given a number of examples of how progress in 3D imaging, through developments in microscopy technique and in novel reconstruction algorithms, can lead to new insights into structure and composition at the nanoscale. The advent of aberration-corrected electron optics has revolutionised the way in which the atomic structure of nanoparticles can be visualised in a direct manner. Examples have been given of how the structure of nanoparticles can be elucidated in exquisite detail, revealing twin boundaries, re-entrant facets and surface-related structral re-arrangement. Individual atoms can be identified with aberration-corrected STEM and, coupled with analytical techniques such as X-ray emission spectroscopy, provides a remarkably powerful instrument for the investigation of nanostructures and a better understanding of their physico–chemical behaviour.

Acknowledgements

CD acknowledges financial support from the Royal Society. PAM acknowledges financial support from the ERC, Reference 291522 3DIMAGE.

References

[1] P.A. Midgley, E.P.W. Ward, A.B. Hungria, J.M. Thomas, Nanotomography in the chemical, biological and materials sciences, Chemical Society Reviews 36 (2007) 1477–1494.
[2] G.-C. Yin, M.-T. Tang, Y.-F. Song, F.-R. Chen, K.S. Liang, F.W. Duewer, et al., Energy-tunable transmission X-ray microscope for differential contrast imaging with near 60 nm resolution tomography, Applied Physics Letters 88 (24) (2006) 241115.
[3] M.A. Le Gros, G. McDermott, C.A. Larabell, X-ray tomography of whole cells, Current Opinion in Structural Biology 15 (5) (2005) 593–600.

[4] J. Radon, Über die Bestimmung von Funktionen durch ihre Integralwerte langs gewisser Mannigfaltigkeiten, Ber Verh K Sachs Ges Wiss Leipzig Math-Phys Kl 69 (1917) 262–277.
[5] S.R. Deans, The Radon Transform and Some of its Applications, Wiley, New York; Chichester, 1983.
[6] G.N. Ramachandran, A.V. Lakshminarayanan, Three-dimensional reconstruction from radiographs and electron micrographs: application of convolutions instead of fourier transforms, Proceedings of the National Academy of Sciences 68 (9) (1971) 2236–2240.
[7] D.J. De Rosier, A. Klug, Reconstruction of three dimensional structures from electron micrographs, Nature 217 (5124) (1968) 130–134.
[8] R.A. Crowther, D.J. DeRosier, A. Klug, The reconstruction of a three-dimensional structure from projections and its application to electron microscopy, Proceedings of the Royal Society of London A 317 (1530) (1970) 319–340.
[9] W. Hoppe, R. Langer, G. Knesch, C. Poppe, Protein-Kristallstrukturanalyse mit Elektronenstrahlen, Naturwissenschaften 55 (7) (1968) 333–336.
[10] M. Radermacher, Weighted back-projection methods, in: J. Frank (Ed.), Electron Tomography: Methods For Three-Dimensional Visualization of Structures In The Cell, Springer, New York; London, 2006, pp. 245–273.
[11] Z. Saghi, D.J. Holland, R. Leary, A. Falqui, G. Bertoni, A.J. Sederman, et al., Three-dimensional morphology of iron oxide nanoparticles with reactive concave surfaces. a compressed sensing-electron tomography (CS-ET) approach, Nano Letters 11 (11) (2011) 4666–4673.
[12] M.C. Scott, C.-C. Chen, M. Mecklenburg, C. Zhu, R. Xu, P. Ercius, et al., Electron tomography at 2.4 Å resolution, Nature 483 (7390) (2012) 444–447.
[13] A.C. Kak, M. Slaney, Principles of computerized tomographic imaging. Philadelphia: Society for Industrial and Applied Mathematics, SIAM, Philadelphia, 2001.
[14] G.T. Herman, Fundamentals of Computerized Tomography: Image Reconstruction from Projections Dordrecht, Springer, Heidelberg; London; New York, 2009.
[15] P.A. Penczek, J.J. Grant, Fundamentals of Three-Dimensional Reconstruction from Projections, in: G.J. Jenson (Ed.), Methods in Enzymology, Academic Press, Amsterdam, 2010, pp. 1–33.
[16] J. Frank, Electron Tomography: Methods for Three-Dimensional Visualization of Structures in the Cell, Springer, New York; London, 2006.
[17] P.F.C. Gilbert, The reconstruction of a three-dimensional structure from projections and its application to electron microscopy. II. Direct methods, Proceedings of the Royal Society B 182 (1066) (1972) 89–102.
[18] S.H. Bellman, R. Bender, R. Gordon, J.E. Rowe, ART is science being a defense of algebraic reconstruction techniques for three-dimensional electron microscopy, J Theor Biol 32 (1) (1971) 205–216.
[19] R.A. Crowther, A. Klug, ART and science or conditions for three-dimensional reconstruction from electron microscope images, Journal of Theoretical Biology 32 (1) (1971) 199–203.
[20] P. Gilbert, Iterative methods for the three-dimensional reconstruction of an object from projections, Journal of Theoretical Biology 36 (1) (1972) 105–117.
[21] M.I. Sezan, An overview of convex projections theory and its application to image recovery problems, Ultramicroscopy 40 (1) (1992) 55–67.
[22] J.-M. Carazo, G.T. Herman, C.O.S. Sorzano, R. Marabini, Algorithms for three-dimensional reconstruction from the imperfect projection data provided by electron microscopy, in: J. Frank (Ed.), Electron Tomography: Methods for Three-Dimensional Visualization of Structures in the Cell, Springer, New York; London, 2006, pp. 217–244.
[23] K.J. Batenburg, S. Bals, J. Sijbers, C. Kübel, P.A. Midgley, J.C. Hernandez, et al., 3D imaging of nanomaterials by discrete tomography, Ultramicroscopy 109 (6) (2009) 730–740.
[24] B. Goris, W. Van den Broek, K.J. Batenburg, H. Heidari Mezerji, S. Bals, Electron tomography based on a total variation minimization reconstruction technique, Ultramicroscopy 113 (2012) 120–130.
[25] G.T. Herman, A. Kuba, Advances in Discrete Tomography and Its Applications, Birkhauser, Boston, 2007.
[26] R. Leary, P.A. Midgley, J.M. Thomas, Recent advances in the application of electron tomography to materials chemistry, Accounts of Chemical Research 45 (10) (2012) 1782–1791.
[27] M. Lustig, D. Donoho, J.M. Pauly, M.R.I. Sparse, The application of compressed sensing for rapid MR imaging, Magnetic Resonance in Medical Sciences 58 (6) (2007) 1182–1195.
[28] E.Y. Sidky, C.-M. Kao, X. Pan, Accurate image reconstruction from few-views and limited-angle data in divergent-beam CT, Journal of X-Ray Science and Technology 14 (2006) 119–139.
[29] E.J. Candès, J. Romberg, T. Tao, Robust uncertainty principles: exact signal reconstruction from highly incomplete frequency information, IEEE Transactions on Information Theory 52 (2) (2006) 489–509.
[30] D.L. Donoho, Compressed sensing, IEEE Transactions on Information Theory 52 (4) (2006) 1289–1306.
[31] C. George, D. Dorfs, G. Bertoni, A. Falqui, A. Genovese, T. Pellegrino, et al., A cast-mold approach to iron oxide and Pt/Iron oxide nanocontainers and nanoparticles with a reactive concave surface, Journal of the American Chemical Society 133 (7) (2011) 2205–2217.
[32] R. Leary, Z. Saghi, P.A. Midgley, D.J. Holland, Ultramicroscopy, (2013), http://dx.doi.org/10.1016/j.ultramic.2013.03.019.
[33] O. Nicoletti, F. de la Peña, R.K. Leary, D.J. Holland, C. Ducati, P.A. Midgley, under review.
[34] C. Burda, X. Chen, R. Narayanan, M.A. El-Sayed, Chemistry and properties of nanocrystals of different shapes, Chemical Reviews 105 (4) (2005) 1025–1102.
[35] E.M. Perassi, J.C. Hernandez-Garrido, M.S. Moreno, E.R. Encina, E.A. Coronado, P.A. Midgley, Using highly accurate 3d nanometrology to model the optical properties of highly irregular nanoparticles: a powerful tool for rational design of plasmonic devices, Nano Lettrs 10 (6) (2010) 2097–2104.
[36] J.M. Thomas, B.F.G. Johnson, R. Raja, G. Sankar, P.A. Midgley, High-performance nanocatalysts for single-step hydrogenations, Accounts of Chemical Research 36 (1) (2003) 20–30.
[37] J.M. Thomas, R. Raja, D.W. Lewis, Single-site heterogeneous catalysts, ChemInform 37 (2) (2006), http://dx.doi.org/10.1002/chin.200602238.
[38] W.Z. Zhou, J.M. Thomas, D.S. Shephard, B.F.G. Johnson, D. Ozkaya, T. Maschmeyer, et al., Ordering of ruthenium cluster carbonyls in mesoporous silica, Science 280 (5364) (1998) 705–708.
[39] E.P.W. Ward, I. Arslan, P.A. Midgley, A. Bleloch, J.M. Thomas, Direct visualisation, by aberration-corrected electron microscopy, of the crystallisation of bimetallic nanoparticle catalysts, Chemical Communications 46 (2005) 5805–5807.
[40] P.A. Midgley, J.M. Thomas, L. Laffont, M. Weyland, R. Raja, B.F.G. Johnson, et al., High-resolution scanning transmission electron tomography and elemental analysis of zeptogram quantities of heterogeneous catalyst, Journal of Physical Chemistry B 108 (15) (2004) 4590–4592.
[41] T.J.V. Yates, J.M. Thomas, J.-J. Fernandez, O. Terasaki, R. Ryoo, P. A. Midgley, Three-dimensional real-space crystallography of MCM-48 mesoporous silica revealed by scanning transmission electron tomography, Chemical Physics Letters 418 (4–6) (2006) 540–543.
[42] Y. Sakamoto, T.-W. Kim, R. Ryoo, O. Terasaki, Three-dimensional structure of large-pore mesoporous cubic Ia$\bar 3$d silica with complementary pores and its carbon replica by electron crystallography, Angewandte Chemie International Edition 43 (39) (2004) 5231–5234.
[43] I. Arslan, J.R. Tong, P.A. Midgley, Reducing the missing wedge: high-resolution dual axis tomography of inorganic materials, Ultramicroscopy 106 (11–12) (2006) 994–1000.
[44] R. Brydson, Aberration-Corrected Analytical Transmission Electron Microscopy, RMS-Wiley, Chichester, 2011.
[45] O.L. Krivanek, M.F. Chisholm, M.F. Murfitt, N. Dellby, Scanning transmission electron microscopy: Albert Crewe's vision and beyond, Ultramicroscopy, 123, 90–98.
[46] S.J. Pennycook, Seeing the atoms more clearly: STEM imaging from the Crewe era to today, Ultramicroscopy 123 (0) (2012) 28–37.
[47] S.J. Pennycook, P.D. Nellist, Scanning Transmission Electron Microscopy, Springer, New York, 2011.
[48] L.D. Marks, Surface structure and energetics of multiply twinned particles, Philosophical Magazine A 49 (1) (1984) 81–93.

[49] S. Ino, Stability of multiply-twinned particles, Journal of the Physical Society of Japan 27 (4) (1969) 941–953.
[50] V.G. Gryaznov, J. Heydenreich, A.M. Kaprelov, S.A. Nepijko, A.E. Romanov, J. Urban, Pentagonal symmetry and disclinations in small particles, Crystal Research and Technology 34 (9) (1999) 1091–1119.
[51] H. Hofmeister, Forty years study of fivefold twinned structures in small particles and thin films, Crystal Research and Technology 33 (1) (1998) 3–25.
[52] L.D. Marks, Experimental studies of small particle structures, Reports on Progress in Physics 57 (6) (1994) 603.
[53] A. Mayoral, H. Barron, R. Estrada-Salas, A. Vazquez-Duran, M. Jose-Yacaman, Nanoparticle stability from the nano to the meso interval, Nanoscale 2 (3) (2010) 335–342.
[54] M.J. Walsh, K. Yoshida, A. Kuwabara, M.L. Pay, P.L. Gai, E.D. Boyes, On the structural origin of the catalytic properties of inherently strained ultrasmall decahedral gold nanoparticles, Nano Letters 12 (4) (2012) 2027–2031.
[55] C. Ducati, D.H. Dawson, J.R. Saffell, P.A. Midgley, Ruthenium-coated ruthenium oxide nanorods, Applied Physics Letters 85 (22) (2004) 5385–5387.
[56] R. Ferrando, J. Jellinek, R.L. Johnston, Nanoalloys: from theory to applications of alloy clusters and nanoparticles, Chemical Reviews 108 (3) (2008) 845–910.
[57] J.K. Norskov, T. Bligaard, J. Rossmeisl, C.H. Christ1ensen, Towards the computational design of solid catalysts, Nature Chemistry 1 (1) (2009) 37–46.
[58] J.H. Sinfelt, Bimetallic Catalysts: Discoveries, Concepts and Applications, Wiley, New York, 1983.
[59] M. Armbrüster, M. Behrens, F. Cinquini, K. Föttinger, Y. Grin, A. Haghofer, et al., How to control the selectivity of palladium-based catalysts in hydrogenation reactions: the role of subsurface chemistry, ChemCatChem 4 (8) (2012) 1048–1063.
[60] M. Armbrüster, K. Kovnir, M. Behrens, D. Teschner, Y. Grin, R. Schlögl, Pd−Ga intermetallic compounds as highly selective semihydrogenation catalysts, Journal of the American Chemical Society 132 (42) (2010) 14745–14747.
[61] R. Leary, F. Dela Peña, J.S. Barnard, Y. Luo, M. Armbrüster, R. Schlögl, et al., Chem Cat Chem (2013), http://dx.doi.org/10.1002/cctc.201300029.
[62] R. Leary, Z. Saghi, M. Armbrüster, G. Wowsnick, R. Schlögl, J.M. Thomas, et al., Quantitative high-angle annular dark-field scanning transmission electron microscope (HAADF-STEM) tomography and high-resolution electron microscopy of unsupported intermetallic $GaPd_2$ catalysts, Journal of Physical Chemistry C 116 (24) (2012) 13343–13352.
[63] K. Kovnir, M. Schmidt, C. Waurisch, M. Armbrüster, Y. Prots, Y. Grin, Refinement of the crystal structure of dipalladium gallium, Pd_2Ga, Zeitschrift für Kristallographie— New Crystal Structures 223 (1) (2008) 7–8.
[64] M. Behrens, F. Studt, I. Kasatkin, S. Kühl, M. Hävecker, F. Abild-Pedersen, et al., The active site of methanol synthesis over Cu/ZnO/Al2O3 industrial catalysts, Science 336 (6083) (2012) 893–897.
[65] A.A. Herzing, C.J. Kiely, A.F. Carley, P. Landon, G.J. Hutchings, Identification of active gold nanoclusters on iron oxide supports for CO oxidation, Science 321 (5894) (2008) 1331–1335.
[66] G. Kyriakou, M.B. Boucher, A.D. Jewell, E.A. Lewis, T.J. Lawton, A.E. Baber, et al., Isolated metal atom geometries as a strategy for selective heterogeneous hydrogenations, Science 335 (6073) (2012) 1209–1212.
[67] P.L. Gai, K. Yoshida, C. Shute, X. Jia, M. Walsh, M. Ward, et al., Probing structures of nanomaterials using advanced electron microscopy methods, including aberration-corrected electron microscopy at the angstrom scale, Microscopy Research and Technique 74 (7) (2011) 664–670.

John Meurig Thomas is Honorary Professor of Solid-State Chemistry at the University of Cambridge. He was educated at the University of Wales and for 20 years taught and researched there before becoming Head of Physical Chemistry at the University of Cambridge (1978–1986). He was Director of the Royal Institution of Great Britain from 1986 to 1991. He is the recipient of numerous prizes, honorary doctorates, and Foreign Fellowships of many universities and academies for his work in solid-state, materials, and surface chemistry, and he has pioneered the use and chemical applications of many facets of electron microscopy and spectroscopy since the mid-1960s